



HAL
open science

Numerical study of unsteady rarefied gas flow through an orifice

M.T. T Ho, Irina Martin Graur

► **To cite this version:**

M.T. T Ho, Irina Martin Graur. Numerical study of unsteady rarefied gas flow through an orifice. Vacuum, 2014, 109, pp.253 - 265. 10.1016/j.vacuum.2014.05.004 . hal-01784154

HAL Id: hal-01784154

<https://hal.science/hal-01784154>

Submitted on 22 May 2018

HAL is a multi-disciplinary open access archive for the deposit and dissemination of scientific research documents, whether they are published or not. The documents may come from teaching and research institutions in France or abroad, or from public or private research centers.

L'archive ouverte pluridisciplinaire **HAL**, est destinée au dépôt et à la diffusion de documents scientifiques de niveau recherche, publiés ou non, émanant des établissements d'enseignement et de recherche français ou étrangers, des laboratoires publics ou privés.

1 Numerical study of unsteady rarefied gas flow through an
2 orifice

3 M.T. Ho, I. Graur

4 *Aix Marseille Université, IUSTI UMR CNRS 7343, 13453, Marseille, France*

5 **Abstract**

Transient flow of rarefied gas through an orifice caused by various pressure ratios between the reservoirs is investigated for a wide range of the gas rarefaction, varying from the free molecular to continuum regime. The problem is studied on the basis of the numerical solution of unsteady S-model kinetic equation. It is found that the mass flow rate takes from 2.35 to 30.37 characteristic times, which is defined by orifice radius over the most probable molecular speed, to reach its steady state value. The time of steady flow establishment and the steady state distribution of the flow parameters are compared with previously reported data obtained by the Direct Simulation Monte Carlo (DSMC) method. A simple fitting expression is proposed for the approximation of the mass flow rate evolution in time.

6 *Keywords:* rarefied gas, kinetic equation, orifice, transient flow

7 **1. Introduction**

8 The nonequilibrium flows of gases appear in different technological domains
9 like the vacuum equipment, high altitude aerodynamics and in a relatively new
10 field as the microelectromechanical systems (MEMS). The deviation of a gas
11 from its local equilibrium state can be characterized by the Knudsen number,
12 which present the ratio between the molecular mean free path and the charac-
13 teristic length of the problem. For the relatively large values of the Knudsen
14 number the classical continuum approach fails to describe the gas behavior and
15 the kinetic equations, like the Boltzmann equation or model kinetic equations,
16 must be solved to simulate the gas flows.

17 The gas flow through a thin orifice is a problem of a large practical interest
18 for the design of the vacuum equipment, space or the microfluidic applications.
19 The under-expanded jets through the orifices are predominately used by par-
20 ticle analyzer systems to separate and isolate molecules, ions of substances for
21 analyzing their physical and chemical properties. The time dependent charac-
22 teristics of these jets are important for the investigation of the response time
23 of the vacuum gauges developed for the measurements of the rapid pressure
24 changes [1].

25 The steady state flows through the orifice, slit and short tube have been
 26 successfully studied applying the DSMC method and the kinetic equations [2],
 27 [3], [4], [5], [6], [7], [8], [9]. However, only a few results on the transient rarefied
 28 flows through an orifice [10], a short tube [11], a long tube [12] or a slit [13]
 29 may be found in open literature. The flow conditions in [10] are limited to
 30 high and moderate Mach number owing to significant statical noise of DSMC
 31 method at low Mach number. The authors of [1] also studied experimentally and
 32 numerically the transient gas flow, but between two tanks of the fixed volumes.
 33 The rapid high amplitude pressure changings in time are examined and their
 34 characteristic time was found to be of the order of few seconds.

35 The aim of this work is to analyze the transient properties of gas flow through
 36 an orifice induced by various values of the pressure ratio over a broad range of
 37 gas rarefaction. The unsteady nonlinear S-model kinetic equation is solved
 38 numerically by Discrete Velocity Method (DVM) to obtain the mass flow rate
 39 and macroscopic parameters as a function of time. The time to reach the steady
 40 state conditions for the mass flow rate is also estimated. An empirical expression
 41 for evaluation of time-dependent mass flow rate is proposed.

42 2. Problem formulation

43 Consider an orifice of radius R_0 contained in an infinitesimally thin wall,
 44 which isolates two infinite reservoirs. Both the upstream and downstream reser-
 45 voirs are filled with a monatomic gas but maintained at different pressures p_0
 46 and p_1 , respectively, with $p_0 > p_1$. The temperatures of the wall and of the gas
 47 in the reservoirs are equal to T_0 . At time $t = 0$, the orifice is opened instantly
 48 and the gas starts to flow from the upstream reservoir to the downstream one.

49 Let us introduce a cylindrical coordinate system (r', ϑ, z') with the origin
 50 positioned at the center of the orifice and the Oz' axis directed along the axis of
 51 the reservoirs (see the lateral section shown in Fig. 1). We assume that the flow
 52 is cylindrically symmetric and does not depend on the angle ϑ and therefore the
 53 problem may be considered as two dimensional in the physical space with the
 54 position vector $\mathbf{s}' = (r', z')$.

55 The gas-surface interaction has a very small impact on an orifice flow [14];
 56 consequently, this flow is governed by two principal parameters: the pressure
 57 ratio p_1/p_0 and gas rarefaction δ determined as

$$\delta = \frac{R_0 p_0}{\mu_0 v_0}, \quad v_0 = \sqrt{\frac{2kT_0}{m}}, \quad (1)$$

58 where μ_0 is the viscosity coefficient at the temperature T_0 , v_0 is the most prob-
 59 able molecular speed at the same temperature; m is the molecular mass of the
 60 gas; k is the Boltzmann constant. It is to note that the gas rarefaction param-
 61 eter is inversely proportional to the Knudsen number; *i.e.*, when δ varies from
 62 0 to ∞ , the flow regime changes from the free molecular to the hydrodynamic
 63 regime.

64 It is convenient to define the characteristic time t_0 of the flow as follows

$$t_0 = \frac{R_0}{v_0}. \quad (2)$$

65 The unsteady S-model kinetic equation [15] is used to simulate the tran-
 66 sient rarefied gas flow through the orifice. The conservative formulation of this
 67 equation [16], [17] is implemented

$$\frac{\partial}{\partial t'} (r' f') + \frac{\partial}{\partial r'} (r' f' v_p \cos \varphi) - \frac{\partial}{\partial \varphi} (f' v_p \sin \varphi) + \frac{\partial}{\partial z'} (r' f' v_z) = r' \nu' (f^{S'} - f'). \quad (3)$$

68 The main unknown is the molecular velocity distribution function $f'(t', \mathbf{s}', \mathbf{v})$,
 69 $\mathbf{v} = (v_p \cos \varphi, v_p \sin \varphi, v_z)$ is the molecular velocity vector representing the
 70 molecular velocity space. The polar coordinates are introduced in a plane
 71 (v_r, v_ϑ) and v_p, φ are the magnitude and orientation of the molecular velocity
 72 vector in this (v_r, v_ϑ) plane. The molecular collision frequency ν' is supposed
 73 to be independent on the molecular velocity and can be evaluated [15] by

$$\nu' = \frac{p'}{\mu'}. \quad (4)$$

74 The equilibrium distribution function $f^{S'}$ [15] in eq. (3) is defined in as

$$f^{S'} = f^{M'} \left[1 + \frac{2m \mathbf{V} \mathbf{q}'}{15n' (kT)^2} \left(\frac{mV^2}{2kT'} - \frac{5}{2} \right) \right], \quad f^{M'} = n' \left(\frac{m}{2\pi kT'} \right)^{3/2} \exp \left(-\frac{mV^2}{2kT'} \right), \quad (5)$$

75 where $f^{M'}$ is the local Maxwellian distribution function, $\mathbf{V} = \mathbf{v} - \mathbf{u}'$ is the pec-
 76 culiar velocity vector, $\mathbf{u}' = (u'_r, 0, u'_z)$ is the bulk velocity vector, $\mathbf{q}' = (q'_r, 0, q'_z)$
 77 is the heat flux vector, n' is the gas numerical density.

78 It is useful to define the dimensionless variables as follows

$$\begin{aligned} t &= \frac{t'}{t_0}, \quad \mathbf{s} = \frac{\mathbf{s}'}{R_0}, \quad \mathbf{c} = \frac{\mathbf{v}}{v_0}, \quad \mathbf{u} = \frac{\mathbf{u}'}{v_0}, \quad n = \frac{n'}{n_0}, \\ T &= \frac{T'}{T_0}, \quad p = \frac{p'}{p_0}, \quad \mathbf{q} = \frac{\mathbf{q}'}{p_0 v_0}, \quad \mu = \frac{\mu'}{\mu_0}, \quad f = \frac{f' v_0^3}{n_0}, \end{aligned} \quad (6)$$

79 with the help of the state equation $p_0 = n_0 k T_0$. In relations (6), the dimension-
 80 less molecular velocity vector \mathbf{c} is equal to $(c_p \cos \varphi, c_p \sin \varphi, c_z)$.

81 In this study, the inverse power law potential is employed as the molecu-
 82 lar interaction potential; therefore, viscosity can be calculated by power law
 83 temperature dependence as

$$\mu = T^\omega, \quad (7)$$

84 where ω is the viscosity index, which is equal to 0.5 for Hard Sphere model and
 85 1 for the Maxwell model [18].

86 Incorporating dimensionless quantities (6) into S-model kinetic equation (3),
 87 the dimensionless conservative form of governing equation is obtained

$$\frac{\partial}{\partial t} (r f) + \frac{\partial}{\partial r} (r f c_p \cos \varphi) - \frac{\partial}{\partial \varphi} (f c_p \sin \varphi) + \frac{\partial}{\partial z} (r f c_z) = r \delta n T^{1-\omega} (f^S - f). \quad (8)$$

88 The above equation is subjected to the following boundary conditions. The
 89 distribution function of outgoing from the axis molecules f^+ is calculated from
 90 the distribution function of incoming to the axis molecules f^- taking into ac-
 91 count the axisymmetric condition as

$$f_{r=0}^+(t, z, r, \varphi, c_p, c_z) = f_{r=0}^-(t, z, r, \pi - \varphi, c_p, c_z), \quad (9)$$

92 where the superscripts + and - refer to the outgoing and incoming molecules,
 93 respectively. It is supposed that the computational domain is large enough for
 94 obtaining the equilibrium far-field. Hence, we assume that the molecules enter-
 95 ing the computational domain are distributed according to the Maxwellian law
 96 with the parameters determined by the zero-flow at the pressure and tempera-
 97 ture corresponding to each reservoir as follows

$$\begin{aligned} f_{r=R_L}^-(t, z, r, \varphi, c_p, c_z) &= f_{z=-Z_L}^-(t, z, r, \varphi, c_p, c_z) = \frac{1}{\pi^{3/2}} \exp(-c_p^2 - c_z^2), \\ f_{r=R_R}^-(t, z, r, \varphi, c_p, c_z) &= f_{z=Z_R}^-(t, z, r, \varphi, c_p, c_z) = \frac{p_1}{\pi^{3/2}} \exp(-c_p^2 - c_z^2), \end{aligned} \quad (10)$$

98 here R_L , R_R and Z_R , Z_L are the radial and axial dimensions of the left and
 99 right reservoirs, respectively.

100 Since the influence of the gas-wall interaction on the flow is weak (see Ref.
 101 [14]), the fully diffuse scattering is implemented for the molecules reflected from
 102 both sides of the wall, which separates the two reservoirs, *i.e.*

$$f_{z=0^\mp, r>1}^+(t, z, r, \varphi, c_p, c_z) = \frac{n_w^\mp}{\pi^{3/2}} \exp(-c_p^2 - c_z^2), \quad (11)$$

103 where the superscripts \mp refers the left (-) and the right (+) sides of the wall.
 104 The unknown values of the number density at the wall surfaces n_w^\mp are found
 105 from the impermeability conditions

$$n_{w, z=0^\mp, r>1}^\mp(t, z, r) = \pm 4\sqrt{\pi} \int_0^\infty \int_0^\pi \int_0^\infty c_z f_{z=0^\mp}^\mp(t, z, r, \varphi, c_p, c_z) d\mathbf{c}, \quad (12)$$

106 where $d\mathbf{c} = c_p dc_p d\varphi dc_z$.

107 The dimensionless macroscopic flow parameters are defined through the dis-
 108 tribution function as follows

$$\begin{aligned} n(t, z, r) &= 2 \int_{-\infty}^\infty \int_0^\pi \int_0^\infty f d\mathbf{c}, & T(t, z, r) &= \frac{4}{3n} \int_{-\infty}^\infty \int_0^\pi \int_0^\infty C f d\mathbf{c}, \\ u_r(t, z, r) &= \frac{2}{n} \int_{-\infty}^\infty \int_0^\pi \int_0^\infty c_p \cos \varphi f d\mathbf{c}, & u_z(t, z, r) &= \frac{2}{n} \int_{-\infty}^\infty \int_0^\pi \int_0^\infty c_z f d\mathbf{c}, \\ q_r(t, z, r) &= 2 \int_{-\infty}^\infty \int_0^\pi \int_0^\infty c_p \cos \varphi C f d\mathbf{c}, & q_z(t, z, r) &= 2 \int_{-\infty}^\infty \int_0^\pi \int_0^\infty c_z C f d\mathbf{c} \end{aligned} \quad (13)$$

109 where $C = (c_p \cos \varphi - u_r)^2 + (c_p \sin \varphi)^2 + (c_z - u_z)^2$.

110 The mass flow rate is practically the most significant quantity of an orifice
111 flow and can be calculated as

$$\dot{M}(t') = 2\pi m \int_0^{R_0} n'(t', 0, r') u'_z(t', 0, r') r' dr'. \quad (14)$$

112 The steady state mass flow rate into vacuum $p_1/p_0 = 0$ under the free molecular
113 flow conditions ($\delta = 0$) was obtained analytically in Refs. [19], [20], [18] as

$$\dot{M}_{fm} = \frac{R_0^2 \sqrt{\pi}}{\nu_0} p_0, \quad (15)$$

114 and this quantity is used as reference value for the reduced mass flow rate

$$W(t') = \frac{\dot{M}(t')}{\dot{M}_{fm}}. \quad (16)$$

115 The dimensionless mass flow rate is obtained by substituting eqs. (6), (14), (15)
116 into eq. (16)

$$W(t) = 4\sqrt{\pi} \int_0^1 n(t, 0, r) u_z(t, 0, r) r dr. \quad (17)$$

117 Initially the upstream and downstream reservoirs, separated by a diaphragm, are
118 maintained at the pressures p_0 and p_1 , respectively, and at the same temperature
119 T_0 . At time $t = 0$, just after the diaphragm opening, the mass flow rate is equal
120 to $W = 1 - p_1/p_0$.

121 In the next sections we present the numerical approach for the solution of
122 the kinetic equation (8).

123 3. Method of solution

124 Firstly, the discrete velocity method (DVM) is used to separate the contin-
125 uum molecular magnitude velocity spaces $c_p = (0, \infty)$, $c_z = (-\infty, \infty)$ in the
126 kinetic equation (8) into discrete velocity sets c_{p_m} , c_{z_n} , which are taken to be
127 the roots of Hermite polynomial. The polar angle velocity space $\varphi = [0, \pi]$ is
128 equally discretized into set of φ_l . Next, the set of independent kinetic equations
129 corresponding to discrete velocity sets c_{p_m} , c_{z_n} is discretized in time and space
130 by Finite difference method (FDM).

131 For each reservoir its radial and axial dimensions are taken here to be equal
132 ($R_L = Z_L$ and $R_R = Z_R$), and equal to D_L and D_R , respectively. The influence
133 of the dimensions D_L and D_R on the macroscopic parameters distribution is
134 discussed in Section 4.6. In the physical space, the uniform grid ($2N_O * N_O$)
135 with square cells is constructed near the orifice ($z = (-1, 1), r = (0, 1)$), where
136 N_O is the number of the grid points through the orifice. At the remaining com-
137 putational domain ($z = (-Z_L, -1) \cup (1, Z_R), r = (1, R_{L/R})$), the non-uniform

138 discretization using increasing power-law of 1.05 is implemented for both radial
 139 and axial directions, as it is illustrated in Fig. 1.

140 The spacial derivatives are approximated by one of two upwind schemes:
 141 the first-order accurate scheme or second-order accurate TVD type scheme.
 142 The time derivative is approximated by the time-explicit Euler method. The
 143 combination of a second-order spatial discretization with forward Euler time-
 144 marching is unstable, according to a linear stability analysis [21]. However the
 145 presence of the non-linear limiter keeps it stable [21], [22]. The details of the
 146 implemented approximations are discussed in Section 4.1.

147 As an example the second-order accurate TVD upwind scheme with the
 148 time-explicit Euler approximation is given for the case of $\cos \varphi_l > 0$, $\sin \varphi_l > 0$
 149 and $c_{z_n} > 0$, when the kinetic equation (8) is replaced by the set of independent
 150 discretized equations

$$\begin{aligned}
 & \frac{r_j f_{i,j,l,m,n}^{k+1} - r_j f_{i,j,l,m,n}^k}{\Delta t^k} + c_{p_m} \cos \varphi_l \frac{F_{i,j+1/2,l,m,n}^k - F_{i,j-1/2,l,m,n}^k}{0.5(r_{j+1} - r_{j-1})} \\
 & - c_{p_m} \frac{f_{i,j,l+1,m,n}^k \sin \varphi_{l+1/2} - f_{i,j,l,m,n}^k \sin \varphi_{l-1/2}}{2 \sin(\Delta \varphi_l / 2)} + c_{z_n} \frac{F_{i+1/2,j,l,m,n}^k - F_{i-1/2,j,l,m,n}^k}{0.5(z_{i+1} - z_{i-1})} \\
 & = r_j \delta n_{i,j}^k (T_{i,j}^k)^{1-\omega} \left((f_{i,j,l,m,n}^S)^k - f_{i,j,l,m,n}^k \right), \tag{18}
 \end{aligned}$$

151 where $f_{i,j,l,m,n}^k = f(t^k, z_i, r_j, \varphi_l, c_{p_m}, c_{z_n})$, $\Delta t^k = t^{k+1} - t^k$, $\Delta z_i = z_i - z_{i-1}$,
 152 $\Delta r_j = r_j - r_{j-1}$, $\Delta \varphi_l = \varphi_l - \varphi_{l-1}$. In eq. (18), the approximation of derivative
 153 of axisymmetric transport term (with respect to φ) is implemented with trigono-
 154 metric correction [23], which helps to reduce considerably the total number of
 155 grid points N_φ in the polar angle velocity space φ .

156 The second-order edge fluxes in the point of physical space i, j are computed
 157 as

$$\begin{aligned}
 & F_{i\pm 1/2,j,l,m,n}^k = f_{i\pm 1/2,j,l,m,n}^k r_j, \quad F_{i,j\pm 1/2,l,m,n}^k = f_{i,j\pm 1/2,l,m,n}^k r_{j\pm 1/2} \tag{19} \\
 & f_{i+1/2,j,l,m,n}^k = \begin{cases} f_{i,j,l,m,n}^k + 0.5 \Delta z_{i+1} \min \text{mod}(D_{i+1/2,j,l,m,n}, D_{i-1/2,j,l,m,n}) & \text{if } c_{z_n} \geq 0 \\ f_{i+1,j,l,m,n}^k - 0.5 \Delta z_{i+1} \min \text{mod}(D_{i+3/2,j,l,m,n}, D_{i+1/2,j,l,m,n}) & \text{if } c_{z_n} < 0, \end{cases} \\
 & f_{i,j+1/2,l,m,n}^k = \begin{cases} f_{i,j,l,m,n}^k + 0.5 \Delta r_{j+1} \min \text{mod}(D_{i,j+1/2,l,m,n}, D_{i,j-1/2,l,m,n}) & \text{if } \cos \varphi_l \geq 0 \\ f_{i,j+1,l,m,n}^k - 0.5 \Delta r_{j+1} \min \text{mod}(D_{i,j+3/2,l,m,n}, D_{i,j+1/2,l,m,n}) & \text{if } \cos \varphi_l < 0. \end{cases} \tag{20}
 \end{aligned}$$

159 where $r_{j+1/2} = 0.5(r_j + r_{j+1})$ and

$$D_{i+1/2,j,l,m,n} = \frac{f_{i+1,j,l,m,n}^k - f_{i,j,l,m,n}^k}{\Delta z_{i+1}}, \quad D_{i,j+1/2,l,m,n} = \frac{f_{i,j+1,l,m,n}^k - f_{i,j,l,m,n}^k}{\Delta r_{j+1}}. \tag{21}$$

160 The slope limiter *minmod* introduced in [24], [21] is given by

$$\min \text{mod}(a, b) = 0.5(\text{sign}(a) + \text{sign}(b)) \min(|a|, |b|). \tag{22}$$

Table 1: Numerical grid parameters

Phase space	Reservoir	Total number of points	
Physical space z, r	Left Right	$N_O = 40$	$N_{zl} \times N_{rl} = 96 \times 96$ $N_{zr} \times N_{rr} = 101 \times 101$
Molecular velocity space φ, c_p, c_z	Left & Right	$N_\varphi \times N_{c_p} \times N_{c_z} = 40 \times 16 \times 16$	

161 The details of computational grid parameters are given in Table 1.

162 Concerning the temporal discretization, the time step should satisfy the
163 classical Courant-Friedrichs-Lewy (CFL) condition [25] and must also be smaller
164 than the mean collision time, or relaxation time, which is inverse of the collision
165 frequency ν . Consequently, the time step must satisfy the following criterion

$$\Delta t \leq CFL / \max_{i,j,l,m,n} \left(\frac{c_{p_m}}{\Delta r_j} + \frac{c_{p_m}}{r_1 \Delta \varphi_l} + \frac{c_{z_n}}{\Delta z_i}, \nu_{i,j} \right). \quad (23)$$

166 As the mass flow rate is the most important characteristic of the flow through
167 an orifice the convergence criterion is defined for this quantity as follows

$$\frac{|W(t^{k+1}) - W(t^k)|}{W(t^k) \Delta t^k} \leq \varepsilon, \quad (24)$$

168 where ε is a positive number and it is taken equal to 10^{-6} . It is to note that this
169 convergence criterion differs from that used in Ref. [13], where the transient flow
170 through a slit is simulated. Here we introduce the time step in the expression of
171 the convergence criterion. It allows us to have the same convergence criterion
172 when the size of the numerical grid in the physical space and consequently the
173 time step according to the CFL condition (23) change. The expression of the
174 convergence criterion (24) may be considered as the criterion on the velocity
175 of the mass flow rate changes. The time moment, when the criterion (24) is
176 achieved, is notified as t_ε and the corresponding mass flow rate as $W = W(t_\varepsilon)$.
177 It is to underline that the mass flow rate was chosen here as the convergence
178 parameter, as it is the most important and useful characteristic of the flow.
179 However the calculation were conducted in the most cases, except $p_1/p_0 = 0.9$
180 and $\delta = 10$, until time equal to 40, when the criterion (24) was already satisfied,
181 in order to observe the steady state flow establishment in the flow field far from
182 the orifice. The comments on the whole steady state flow field establishment
183 are given in Section 4.3.

184 The numerical method is implemented as follows. First, the distribution
185 function $f_{i,j,l,m,n}^{k+1}$ in the internal grid points at the new time step $k + 1$ is
186 calculated explicitly by eq. (18) from the data of the current time step k .
187 At the boundaries, the distribution function is calculated using the boundary
188 conditions (9) - (11). Once the distribution function is known, the values of
189 the macroscopic parameters for the new time step are obtained by evaluating
190 the integrals in eqs. (13). To do that, the Gauss-Hermite quadrature formulas
191 are applied to calculate the integrals over c_p, c_z spaces, while the trapezoidal

192 rule is used for the approximation of the integrals over φ space. After that, the
193 mass flow rate for the new time step is evaluated by applying the trapezoidal
194 rule for the integral in eq. (17). The macroscopic parameters and the mass
195 flow rate are recorded as a function of time. This procedure is iterated until the
196 convergence criterion (24) is met; *i.e.*, steady flow conditions for the mass flow
197 rate are reached.

198 It is to be noticed that the problem is six dimensional in the phase space:
199 two variables in the physical space, three variables in the molecular velocity
200 space and the time. In order to obtain the reasonable computational time the
201 numerical code is parallelized by using the OpenMP technology. From the
202 resolution of system (18) the velocity distribution function f can be calculated
203 at the new time level separately for each value of the molecular velocity, so
204 these calculations are distributed among the separated processors units. The
205 final results on the macroscopic parameters are obtained by the summation of
206 the corresponding quantities over all processors.

207 The parallelization gives the opportunity to run the program code on multi-
208 core processor. To have an estimation about computational effort and speedup,
209 the wall-clock times for executing the numerical code are recorded. The second-
210 order accurate TVD scheme requires 434 seconds for the first 100 time steps with
211 8 cores of processors AMD 8435 2600MHz and 4Gb of memory for each core,
212 whereas the first-order accurate scheme takes 242 seconds for the same task.
213 These wall-clock times are 2585 and 1518 seconds for second-order accurate TVD
214 scheme and first-order accurate scheme, respectively, when only 1 core is used.

215 4. Numerical results

216 The numerical simulations are conducted for four values of the pressure
217 ratio $p_1/p_0 = 0, 0.1, 0.5, 0.9$ which correspond to flow into vacuum, flow of
218 strong, medium and weak non-equilibrium. For each value of pressure ratio
219 p_1/p_0 the calculations are carried out with four values of rarefaction parameter
220 $\delta = 0.1, 1, 10, 100$; *i.e.*, from the near free molecular to hydrodynamic flow
221 regimes.

222 4.1. Different approximations of the spatial derivatives

223 Two numerical schemes are implemented for the approximation of the spatial
224 derivatives: the first-order accurate scheme and the TVD scheme with *minmod*
225 slope limiter. The CFL number for both schemes was equal to 0.95. The
226 computational time per time step by using the same computational grid is in
227 70% longer for TVD scheme than for the first-order accurate scheme. However,
228 in order to reach the same uncertainty of the mass flow rate the four times
229 larger number of grid points in each dimension of physical space is needed for
230 the first-order accurate scheme, $N_O = 160$, instead of 40 for the TVD scheme.
231 Therefore all simulations are carried out by using the TVD scheme.

232 After the various numerical tests the optimal dimensions of the numerical
233 grid are found (shown in Table 1), which guarantee the numerical uncertainty for

Table 2: Dimensionless flow rate W (17) vs rarefaction parameter δ and pressure ratio p_1/p_0 . Present results $W = W(t_\varepsilon)$, the results from Ref. [5] (W^a), where the steady BGK-model kinetic equation was solved using the fixed point method, the results obtained in Ref. [14] (W^b) by the DSMC technique.

δ	$p_1/p_0 = 0.$			0.1		0.5			0.9		
	W	W^a	W^b	W	W^b	W	W^a	W^b	W	W^a	W^b
0.1	1.020	1.020	1.014	0.919	0.91	0.515	0.515	0.509	0.1039	0.105	0.1025
1.	1.150	1.152	1.129	1.054	1.032	0.636	0.635	0.613	0.1356	0.140	0.1297
10.	1.453	1.472	1.462	1.427	1.435	1.188	1.216	1.188	0.4009	0.432	0.4015
100.	1.527	1.508	1.534	1.519	1.524	1.339	1.325	1.344	0.6725	0.669	0.6741

234 the mass flow rate of the order of 1%. The time step, determined by eq. (23),
235 depends crucially on the classical CFL condition subjected to the additional
236 restriction for the time step to be smaller than the mean collision time. However,
237 for the chosen numerical grid in the physical space, see Table 1, the latter
238 restriction is satisfied automatically. Therefore a unique time step $\Delta t = 0.1543 \times$
239 10^{-4} is used for all the presented here cases.

240 4.2. Mass flow rate

241 The steady-state values of the mass flow rate $W = W(t_\varepsilon)$ are presented
242 in Table 2. These values are in good agreement with the results of Refs. [5],
243 [14], obtained from the solution of the stationary BGK-model kinetic equation
244 by the fixed point method [5] and by applying the DSMC approach [14]. The
245 discrepancy is less than 5% for all considered cases.

246 The values of mass flow rate $W(t)$ at several time moments, from $t = 0$ to
247 ~ 40 , are given in Table 3. The column (t_ε) corresponds to the time needed to
248 reach the convergence criterion (24).

249 To have an estimation of the computational efforts required to achieve the
250 convergence criterion (24) the corresponding dimensionless time t_ε and the number
251 of the time steps are presented in Tables 3 and 4, respectively. The time
252 evolution of the residual, defined according to eq. (24), is shown on Fig. 2 for
253 different pressure ratios to illustrate the convergence velocity of the numerical
254 technique. The slowest convergence rate for $p_1/p_0 = 0$ and 0.1 is corresponding
255 to hydrodynamic regime, whilst that for $p_1/p_0 = 0.5$ and 0.9 is in slip regime.
256 Nevertheless, the fastest convergence rate is observed at transitional regime for
257 all pressure ratios.

258 The evolution of the mass flow rate $W(t)$ to its steady state value (given in
259 Table 3) is also demonstrated in Fig. 3 for different pressure ratios. The time
260 interval shown in Fig. 3 is restricted to the time equal to 40 even if the flow
261 does not completely establish for this time moment in the case of pressure ratio
262 equal to 0.9. The common behavior is observed for the pressure ratios 0 and
263 0.1 with relatively rapid mass flow rate establishment. It is to note that, in the
264 hydrodynamic regime, the slope of the mass flow rate evolution reduces sharply
265 for the both pressure ratios near the time equal to 3 whilst this slope reduction
266 is smooth for other pressure ratios. We can observe anew the longer time of the

267 steady state flow establishment for $p_1/p_0 = 0.9$ in whole range of the rarefaction
 268 parameter, see Fig. 3d).

269 In the hydrodynamic flow regime the mass flow rate has a maximum, than
 270 it decreases to reach after its steady state value from above. This tendency is
 271 visible in the hydrodynamic regime, but the same trend appears in all other
 272 regimes, though there it is less apparent because the amplitude of the mass flow
 273 rate changes is smaller. The non monotone behavior of the residual, see Fig.
 274 2, confirms the oscillatory character of the mass flow rate conducting in time.
 275 This behavior is related to the propagation of the initial perturbations created
 276 by the orifice opening toward the boundary of the computational domain. It is
 277 to note that the similar behavior of the mass flow rate was observed also in Ref.
 278 [11].

279 To characterize the mass flow rate evolution in time we introduce also the
 280 time t_s as a last time moment when the mass flow rate differs by 1% from
 281 its steady state value $W(t_\varepsilon)$. The values of t_s for various pressure ratios and
 282 the rarefaction parameters are provided in Table 3. The two main trends for
 283 time t_s , column (t_s) in Table 3, are found: for the pressure ratios 0, 0.1 and
 284 0.5 the longest time to reach the steady state is needed under the transitional
 285 flow regime ($\delta = 1$), whilst for the pressure ratio 0.9 this maximum of time t_s
 286 appears in the slip flow regime ($\delta = 10$). For the all considered pressure ratios
 287 the minimum of t_s corresponds to the near free molecular flow regime ($\delta = 0.1$).
 288 It is to note that the exceptionally long time to steady state flow establishment
 289 is found in the case $p_1/p_0 = 0.9$ and ($\delta = 10$).

290 The time to steady state mass flow rate establishment, t_s , is compared to
 291 the corresponding quantity t_s^* , obtained by DSMC method in Ref. [11], see the
 292 last column of Table 3. The values of t_s^* provided in Ref. [11] are slightly smaller
 293 than those obtained in the present simulations. The largest difference between
 294 two values in more than 2 times, corresponds to the pressure ratio equal to 0.5
 295 in the near hydrodynamic regime ($\delta = 100$), see Table 3. It is noteworthy that
 296 due to the statistical scattering of the DSMC technique the estimation of the
 297 time to establish the steady flow is more difficult from the DSMC results than
 298 by applying the DVM method.

299 From dimensionless time t_s provided in Table 3, one can calculate easily
 300 the dimensional time t'_s needed to obtain the steady-state mass flow rate by
 301 using eqs. (1), (2), (6). For example, He at room temperature $T_0 = 300K$ has
 302 the most probable molecular speed $v_0 = 1116.05m/s$ and viscosity coefficient
 303 $\mu_0 = 1.985 \times 10^{-5} Nsm^{-2}$ (provided in [18]). If one consider an orifice of
 304 the radius $R_0 = 0.5mm$ and pressure in the upstream reservoir $p_0 = 44.31Pa$,
 305 the gas flow is in transitional regime ($\delta = 1$). The dimensionless time of the
 306 expansion into vacuum (case $p_1/p_0 = 0$ in Table 3) is equal to 6.95 and the
 307 corresponding dimensional time is $3.11\mu s$.

308 The mass flow rate as a function of time was fitted using the following model

$$W(t) = W_{t=0} + (W_{t=t_\varepsilon} - W_{t=0}) (1 - \exp(-t/\tau)), \quad (25)$$

309 where the value at the time moment $t = 0$ is calculated as $W_{t=0} = 1 - p_1/p_0$ and
 310 $W_{t=t_\varepsilon}$ is the value of the mass flow rate corresponding to the time moment $t = t_\varepsilon$

Table 3: Mass flow rate W for different time moments. The time t_s of the steady state flow establishment as a function of the rarefaction parameter δ and the pressure ratio p_1/p_0 ; t_s^* corresponds to the data from Ref. [11]. Time t_s is here the dimensionless value, obtained using eqs. (2) and (6).

p_1/p_0	δ	W						t_ε	t_s	t_s^*
		$t = 0$	1	5	10	20	40			
0.	0.1	1.0	1.003	1.016	1.019	1.020	1.020	19.71	2.35	
	1.	1.0	1.028	1.126	1.146	1.149	1.148	15.77	6.95	
	10.	1.0	1.120	1.423	1.455	1.453	1.456	20.60	6.15	
	100.	1.0	1.171	1.511	1.528	1.522	1.527	35.26	5.07	
0.1	0.1	0.9	0.903	0.915	0.918	0.919	0.919	20.48	2.61	
	1.	0.9	0.928	1.027	1.049	1.054	1.053	16.87	7.84	6.4
	10.	0.9	1.035	1.383	1.427	1.427	1.429	20.94	7.05	7.3
	100.	0.9	1.145	1.500	1.520	1.514	1.519	26.94	5.24	4.4
0.5	0.1	0.5	0.503	0.512	0.514	0.515	0.515	22.39	3.64	
	1.	0.5	0.523	0.607	0.629	0.635	0.635	18.76	9.91	8.7
	10.	0.5	0.623	1.060	1.177	1.191	1.189	26.94	9.84	9.1
	100.	0.5	0.756	1.309	1.351	1.339	1.342	23.59	5.54	14.0
0.9	0.1	0.1	0.1007	0.1030	0.1036	0.1039	0.1039	22.82	4.44	
	1.	0.1	0.1059	0.1275	0.1338	0.1356	0.1354	19.20	10.83	
	10.	0.1	0.1292	0.2602	0.3396	0.3893	0.3991	152.6	30.37	
	100.	0.1	0.1571	0.4248	0.6222	0.6943	0.6727	36.10	12.28	

Table 4: Number of time steps to satisfy convergence criterion (24)

δ	Total number of time steps N ($\times 100$)			
	$p_1/p_0 = 0.$	0.1	0.5	0.9
0.1	1277	1327	1451	1479
1.	1022	1093	1216	1244
10.	1335	1357	1746	9889
100.	2285	1746	1529	1339

311 where the convergence criterion (24) is achieved. Both the values are given in
 312 Tables 2 and 3. The fitting parameter (characteristic time) τ for various pressure
 313 ratios and rarefaction parameters are provided in Table 5 with the corresponding
 314 uncertainty. It is to note that very similar values of τ are found for the pressure
 315 ratios 0 and 0.1 for all rarefaction range. For the pressure ratios 0.5 and 0.9
 316 and for the high level of gas rarefaction also the similar values of the fitting
 317 parameter τ are found. However in the slip and hydrodynamic flow regimes
 318 these values become larger, see Table 5.

319 Figure 4 demonstrates that the exponential representation in form of eq.
 320 (25) gives the good estimation for the time evolution of the mass flow rate.
 321 The coefficient of determination R^2 of the fitting curve is equal, for example, to
 322 0.990 for the case $p_1/p_0 = 0.9$ and $\delta = 1$ and decreases to 0.973 for $p_1/p_0 = 0.9$
 323 and $\delta = 100$. The maximal difference between the values of the mass flow rate,
 324 given by the fitting curve and by the numerical solution of the S-model kinetic
 325 equation, is less than 5% for the case $p_1/p_0 = 0.9$ and $\delta = 100$ and it is of the
 order of 0.3% for the same pressure ratio and $\delta = 1$.

Table 5: Characteristic time τ with 99% confidence interval obtained from fit model eq. (25)

δ	Characteristic time τ			
	$p_1/p_0 = 0.$	0.1	0.5	0.9
0.1	3.415 ± 0.029	3.484 ± 0.028	3.546 ± 0.024	3.561 ± 0.023
1.	2.940 ± 0.034	3.112 ± 0.031	3.429 ± 0.028	3.551 ± 0.028
10.	2.286 ± 0.032	2.393 ± 0.030	3.269 ± 0.039	6.459 ± 0.013
100.	1.879 ± 0.032	1.731 ± 0.019	2.072 ± 0.037	5.597 ± 0.083

326

327 4.3. Flow field

328 After the diaphragm opening the gas starts to flow toward the downstream
 329 reservoir. However, even in the upstream reservoir the flow field becomes per-
 330 turbed from its initial state. From the near free molecular ($\delta = 0$) to the slip
 331 flow regime ($\delta = 10$) for all considered pressure ratios $p_1/p_0 = 0 - 0.9$ the time
 332 behavior of the macroscopic parameters are very similar. The two typical ex-
 333 amples of the macroscopic parameters variation in time are presented in Fig. 5
 334 for the cases $p_1/p_0 = 0.1$ and 0.5 and $\delta = 1$. The number density n smoothly
 335 changes from its value in the upstream reservoir to its downstream value. The
 336 temperature drops through the orifice due to the flow acceleration and increases
 337 up to its initial value far from the orifice in the downstream reservoir. The
 338 temperature drop is larger for the smaller values of the pressure ratio: the tem-
 339 perature decreasing just after the orifice is of the order of 25% for $p_1/p_0 = 0.1$
 340 and $\delta = 1$ and it becomes very small (less than 1%) when the pressure ratio
 341 increases up to 0.9. The macroscopic flow velocity increases through the ori-
 342 fice and its rise depends also on the pressure ratio: for the smaller value of
 343 the pressure ratio the flow acceleration is higher. Far from the orifice in the
 344 upstream and downstream reservoirs the flow velocity goes down to zero. It is
 345 to note that for the larger pressure ratio $p_1/p_0 = 0.9$ even in the case of the

346 near hydrodynamic flow regimes, $\delta = 100$, the time dependent behaviors of the
 347 macroscopic parameters are similar to the previously described.

348 The results obtained in Ref. [26] by using the DSMC technique are also
 349 shown in Fig. 5. The provided here DSMC data correspond to the steady state
 350 solution. Its is clear that the both techniques give very similar results. Only
 351 the temperature behaviors for $p_1/p_0 = 0.5$ are slightly different which can be
 352 related to the influence of the boundary conditions in the downstream reservoir.

353 4.4. Near hydrodynamic regime

354 Completely different behavior is observed for the all considered pressure
 355 ratios, except the case of $p_1/p_0 = 0.9$, in the near hydrodynamic flow regime
 356 ($\delta = 100$). For the pressure ratio $p_1/p_0 = 0.5$, see Fig. 6, the shock wave
 357 appears in the right reservoir and it moves toward the downstream boundary.

358 For the pressure ratio ($p_1/p_0 = 0.1$) the particular flow behavior is observed:
 359 the spatial cell structure of axisymmetric mildly under-expanded jet appears,
 360 formed by the system of incident and reflected shock and compression waves,
 361 see Fig. 7. The distribution of the macroscopic flow parameters for this case
 362 is shown on Fig. 8. In contrast with the previous case, the first cell shock
 363 structure does not move and the second shock wave forms after the first one
 364 with time. The shock wave position may be determined by the maximum of the
 365 number density gradient which is located at $z_M/R_0 = 4.31$. This position can
 366 be estimated also from the empirical relation [27]

$$z_M/R_0 = 1.34\sqrt{p_0/p_1}, \quad (26)$$

367 which predicts the Mach disk location at $z_M/R_0 = 4.24$ from the orifice, so very
 368 good agreement is found between the numerical result and empirical relation
 369 (26).

370 The streamlines for the case $p_1/p_0 = 0.1$ are provided in Fig. 9. It can
 371 be seen that the flow field is non symmetric and that the streamlines are not
 372 parallel to the axis of symmetry.

373 In the case of the gas expansion into vacuum ($p_1/p_0 = 0$) the shock wave
 374 does not appear any more. Expression (26) predicts also that the shock wave
 375 position tends to infinity ($z_M/R_0 \rightarrow \infty$). In this case the flow velocity reach its
 376 maximal value, which depends only on the gas temperature in the inlet reservoir.
 377 Under the hypothesis of the adiabatic expansion and the energy conservation
 378 the following expression for the macroscopic velocity was obtained in Ref. [28]:

$$u_{z_{max}} = \sqrt{\frac{5kT_0}{m}}. \quad (27)$$

379 The numerical value of the maximal macroscopic velocity is equal to 1.588 which
 380 is very close to that predicted by eq. (27).

381 4.5. Choked conditions

382 It is well known that a choked flow is a limiting condition which occurs
 383 when the mass flow rate will not increase with a further decrease in the down-
 384 stream pressure environment while upstream pressure is fixed [29]. Under the

385 conditions $p_1/p_0 < (p_1/p_0)_*$, where $(p_1/p_0)_*$ is the critical pressure ratio, the
 386 further decrease in the downstream pressure reservoir does not lead to the in-
 387 crease of the mass flow rate and the flow becomes "choked". However, for the
 388 case of the flow through a thin orifice the flow never becomes "choked". For
 389 the first time it was discovered in Ref. [30] in the case of the flow through a thin,
 390 square-edged orifice. Finally the physical point at which the choking occurs for
 391 adiabatic conditions is that the exit plane velocity is at sonic conditions. But
 392 in the case of the thin orifice flow the "sonic surface" has a convex shape and
 393 located in the downstream reservoir, see Fig. 10, where two cases of the pres-
 394 sure ratio $p_1/p_0 = 0$ and 0.1 are shown. Therefore the flow is not sonic through
 395 the orifice and it does not becomes really choked: the mass flow rate continue
 396 to increases when pressure ratio decreases, see Table 3 and Fig. 11, especially
 397 for the low values of the rarefaction parameter. The evaluation in time of the
 398 temperature and Mach number profiles in the orifice section are shown on Fig.
 399 12, where one can see that the flow remains subsonic through the orifice with
 400 the maximum velocity near the orifice wall.

401 *4.6. Influence of the computational domain dimensions*

402 The study of an influence of the computational domain dimensions on the
 403 numerical results is carried out and the optimal dimensions of the left and right
 404 reservoirs are found as $D_L = 8$ and $D_R = 10$, respectively.

405 Fig. 13 shows the comparison of the macroscopic profiles evolution in time
 406 along the symmetrical axis for $p_1/p_0 = 0.1$ and $\delta = 100$ obtained for two sizes
 407 of the downstream reservoir $D_R = 10$ and 20 . It is clear from these results
 408 that the both solutions coincide until distance $z/R_0 \sim 8$ from the orifice and
 409 that the mass flow rate evolution is not affected at all by the dimension of the
 410 right computational domain. It is interesting to note that in the case of the
 411 flow through a slit much more larger computational domain must be chosen to
 412 obtain the numerical solution independent from the size of the computational
 413 domain.

414 **5. Conclusion**

415 Transient flow of rarefied gas through an orifice is studied on the basis of
 416 nonlinear S-model kinetic equation. The simulations are conducted from the free
 417 molecular to hydrodynamic regimes for four values of pressure ratio between
 418 reservoirs. The mass flow rate evolution in time is analyzed and it is found
 419 that the time to reach the steady state mass flow rate depends essentially on
 420 the pressure ratio between the reservoirs and on the gas flow regime in the left
 421 reservoir. It needs from 2.35 to 30.37 characteristic times to obtain the steady
 422 state mass flow rate, the maximal time to reach the steady state is found in the
 423 slip regime for the largest pressure ratio 0.9. The simple fitting formula for the
 424 time dependence of the mass flow rate is proposed. It is shown numerically that
 425 the flow through the thin orifice never becomes really choked.

426 6. Acknowledgment

427 This work was granted access to the HPC resources of Aix-Marseille Uni-
428 versité financed by the project Equip@Meso (ANR-10-EQPX-29-01) of the pro-
429 gram "Investissements d'Avenir" supervised by the Agence Nationale pour la
430 Recherche. The authors thank Y. Jobic for ensuring the perfect performance of
431 the cluster at IUSTI Laboratory. We thank Prof. F. Sharipov for providing the
432 DSMC results from Ref. [11].

- 433 [1] K. Jousten, S. Pantazis, J. Buthing, R. Model, M. Wuest, A standard to
434 test the dynamics of vacuum gauges in the millisecond range, *Vacuum* 100
435 (2014) 14–17.
- 436 [2] T. Lilly, S. Gimelshein, A. Ketsdever, G. N. Markelov, Measurements and
437 computations of mass flow and momentum flux through short tubes in
438 rarefied gases, *Phys. Fluids* 18 (9) (2006) 093601.1–11.
- 439 [3] S. Varoutis, D. Valougeorgis, F. Sharipov, Simulation of gas flow through
440 tubes of finite length over the whole range of rarefaction for various pressure
441 drop ratios, *J. Vac. Sci. Technol. A* 22 (6) (2009) 1377–1391.
- 442 [4] I. Graur, A. P. Polikarpov, F. Sharipov, Numerical modelling of rarefied
443 gas flow through a slit at arbitrary gas pressure ratio based on the kinetic
444 equations, *ZAMP* 63 (3) (2012) 503–520.
- 445 [5] S. Misdanitis, S. Pantazis, D. Valougeorgis, Pressure driven rarefied gas
446 flow through a slit and an orifice, *Vacuum* 86 (11) (2012) 1701 – 1708.
- 447 [6] V. V. Aristov, A. A. Frolova, S. A. Zabelok, R. R. Arslanbekov, V. I.
448 Kolobov, Simulations of pressure-driven flows through channels and pipes
449 with unified flow solver, *Vacuum* 86 SI (11) (2012) 1717–1724.
- 450 [7] V. A. Titarev, E. M. Shakhov, Computational study of a rarefied gas flow
451 through a long circular pipe into vacuum, *Vacuum* 86 (11) (2012) 1709–
452 1716.
- 453 [8] V. A. Titarev, Rarefied gas flow in a circular pipe of finite length, *Vacuum*
454 94 (2013) 92–103.
- 455 [9] V. Titarev, E. Shakhov, S. Utyuzhnikov, Rarefied gas flow through a di-
456 verging conical pipe into vacuum, *Vacuum* 101 (0) (2014) 10 – 17.
- 457 [10] F. Sharipov, Transient flow of rarefied gas through an orifice, *J. Vac. Sci.*
458 *Technol. A* 30 (2) (2012) 021602.1–5.
- 459 [11] F. Sharipov, Transient flow of rarefied gas through a short tube, *Vacuum*
460 90 (2013) 25–30.
- 461 [12] J. Lihnaropoulos, D. Valougeorgis, Unsteady vacuum gas flow in cylindrical
462 tubes, *Fusion Engineering and Design* 86 (2011) 2139–2142.

- 463 [13] A. Polikarpov, I. Graur, Unsteady rarefied gas flow through a slit, *Vacuum*
464 101 (2014) 79 – 85. doi:<http://dx.doi.org/10.1016/j.vacuum.2013.07.006>.
- 465 [14] F. Sharipov, Numerical simulation of rarefied gas flow through a thin orifice,
466 *Journal of Fluid Mechanics* 518 (2004) 35–60.
- 467 [15] E. M. Shakhov, Generalization of the Krook kinetic relaxation equation,
468 *Fluid Dyn.* 3 (5) (1968) 95–96.
- 469 [16] I. N. Larina, V. A. Rykov, A numerical method for calculationg axisymmet-
470 ric rarefied gas flows, *Comput. Math. Math. Phys.* 38 (8) (1998) 1335–1346.
- 471 [17] I. Graur, M. T. Ho, M. Wuest, Simulation of the transient heat transfer
472 between two coaxial cylinders, *Journal of Vacuum Science & Technology*
473 *A: Vacuum, Surfaces, and Films* 31 (6) (2013) 061603.1–9.
- 474 [18] G. A. Bird, *Molecular Gas Dynamics and the Direct Simulation of Gas*
475 *Flows*, Oxford Science Publications, Oxford University Press Inc., New
476 York, 1994.
- 477 [19] R. Narasimha, Orifice flow of high Knudsen numbers, *J. Fluid Mech.* 10
478 (1961) 371–384.
- 479 [20] D. R. Willis, Mass flow through a circular orifice and a two-dimensional
480 slit at high Knudsen numbers., *J. Fluid Mech.* 21 (1965) 21–31.
- 481 [21] V. P. Kolgan, Application of the principle of minimizing the derivative to
482 the construction of finite-difference schemes for computing discontinuous
483 solutions of gas dynamics, *Journal of Computational Physics* 230 (7) (2011)
484 2384–2390.
- 485 [22] B. Van Leer, A historical oversight: Vladimir P. Kolgan and his high-
486 resolution scheme, *Journal of Computational Physics* 230 (7) (2011) 2387–
487 2383.
- 488 [23] L. Mieussens, Discrete-velocity models and numerical schemes for the
489 Boltzmann-bgk equation in plane and axisymmetric geometries, *J. Comput.*
490 *Phys.* 162 (2) (2000) 429–466.
- 491 [24] P. L. Roe, Characteristic-based schemes for the euler equations, *Ann. Rev.*
492 *Fluid Mech* 18 (1986) 337–365.
- 493 [25] R. Courant, K. Friedrichs, H. Lewy, On the partial difference equations of
494 mathematicalphysics, *IBM Journal on Research and development* 11 (2)
495 (1967) 215–234.
- 496 [26] F. Sharipov, Benchmark problems in rarefied gas dynamics, *Vacuum* 86
497 (2012) 1697–1700.

- 498 [27] H. Ashkenas, F. S. Sherman, The structure and utilization of supersonic free
 499 jets in low density wind tunnels, in: Proceedings of the 4th International
 500 Symposium on RGD, Vol. 2, 1964, pp. 84–105.
- 501 [28] M. D. Morse, Experimental methods in the physical sciences, Vol. 29B,
 502 Academic Press Inc., 1996, Ch. Supersonic beam sources, pp. 21–47.
- 503 [29] L. Driskell, Control-valve selection and sizing, Research Triangle Park, N.C.
 504 : Instrument Society of America, 1983.
- 505 [30] R. G. Cunningham, Orifice meters with supercritical compressible flow,
 506 Transactions of the ASME 73 (1951) 625–638.

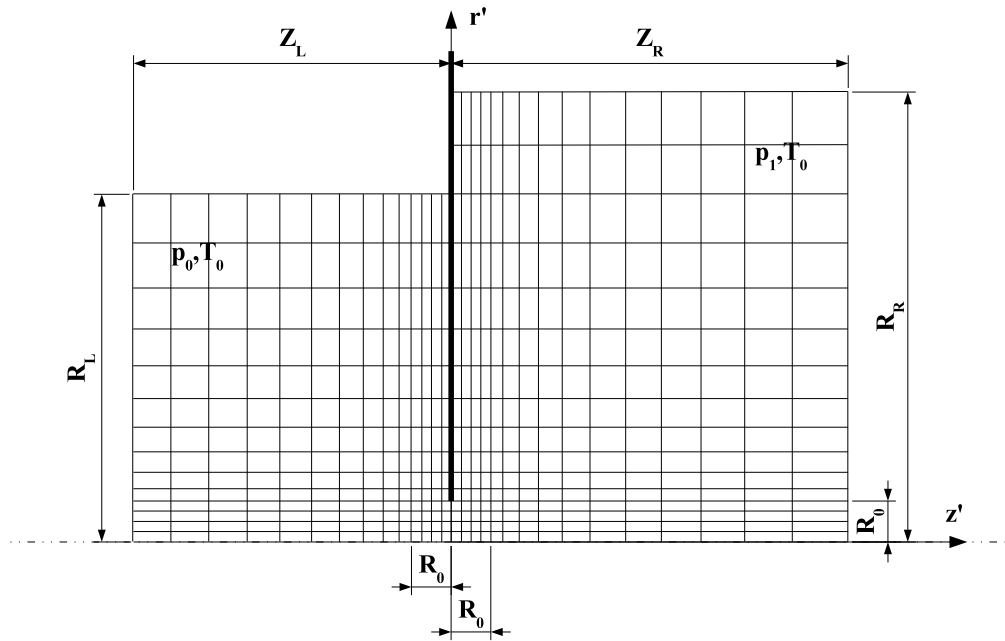


Figure 1: Lateral section and computational domain of the flow configuration

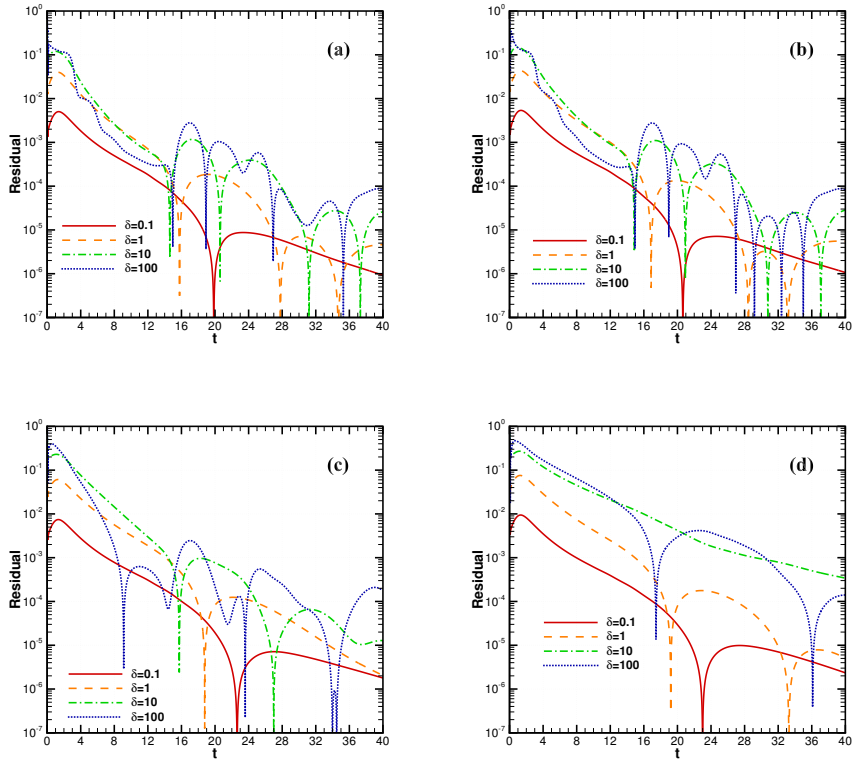


Figure 2: The time evolution of residual for $p_1/p_0 = 0$. (a), $p_1/p_0 = 0.1$ (b), $p_1/p_0 = 0.5$ (c), $p_1/p_0 = 0.9$ (d)

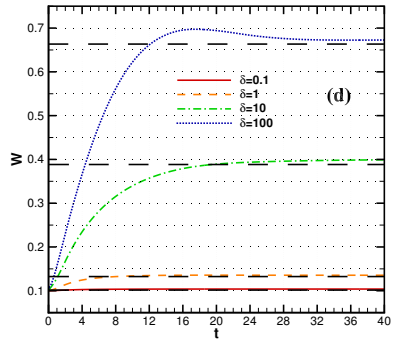
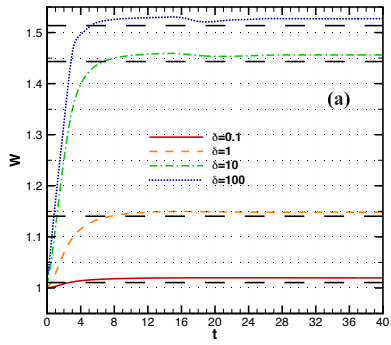


Figure 3: The time evolution of mass flow rate W (solid line) and steady state solution (dashed line) for $p_1/p_0 = 0$. (a), $p_1/p_0 = 0.1$ (b), $p_1/p_0 = 0.5$ (c), $p_1/p_0 = 0.9$ (d)

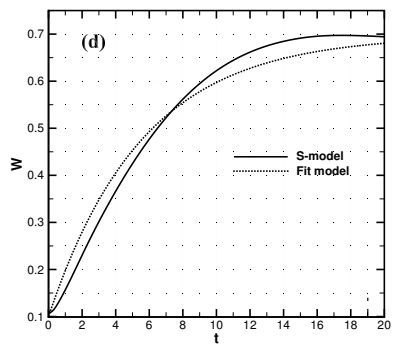


Figure 4: The time evolution of mass flow rate W (solid line) obtained from S-model and fit model eq. (25) for $p_1/p_0 = 0., \delta = 1.$ (a), $p_1/p_0 = 0., \delta = 100.$ (b), $p_1/p_0 = 0.9, \delta = 1.$ (c), $p_1/p_0 = 0.9, \delta = 100.$ (d)

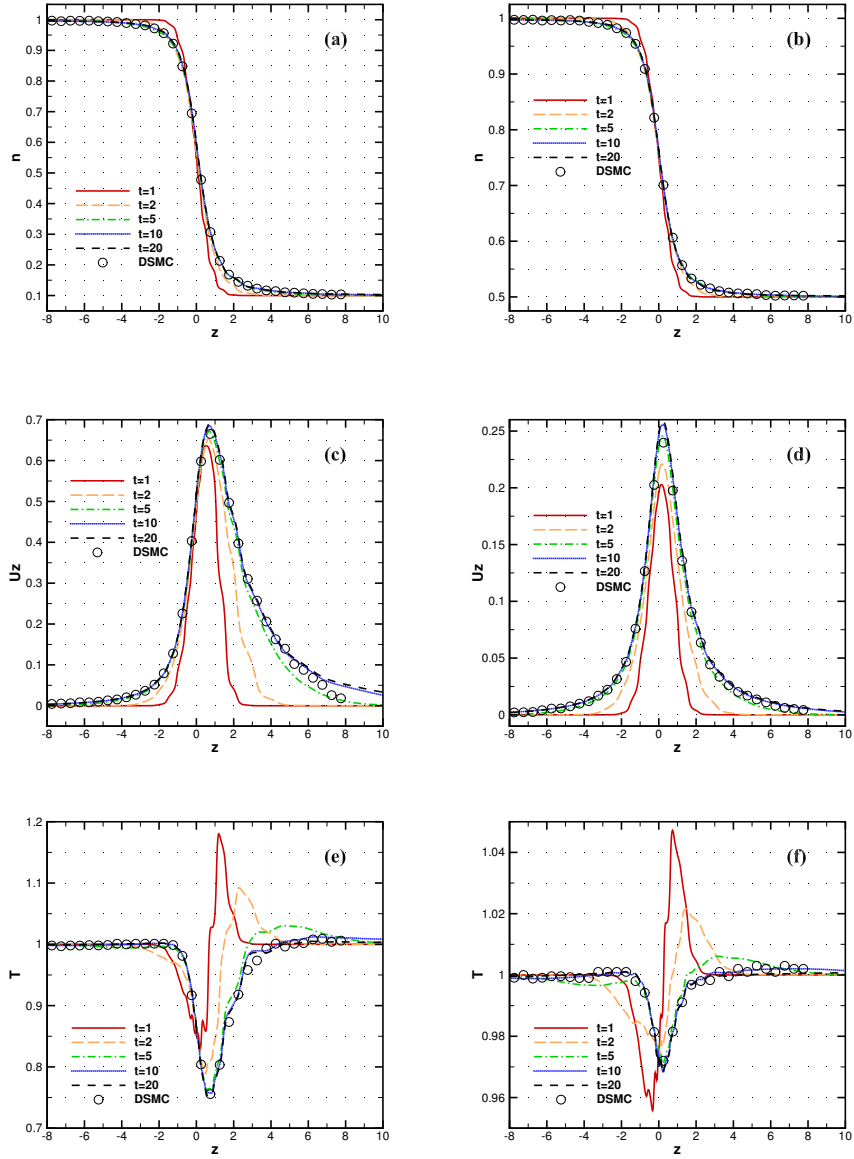


Figure 5: Distribution of density number (a,b), axial velocity (c,d), temperature (e,f) along the axis at several time moments for $p_1/p_0 = 0.1, \delta = 1$. (a,c,e) and $p_1/p_0 = 0.5, \delta = 1$. (b,d,f). The hollow circles correspond to the results obtained in [10] by DSMC method.

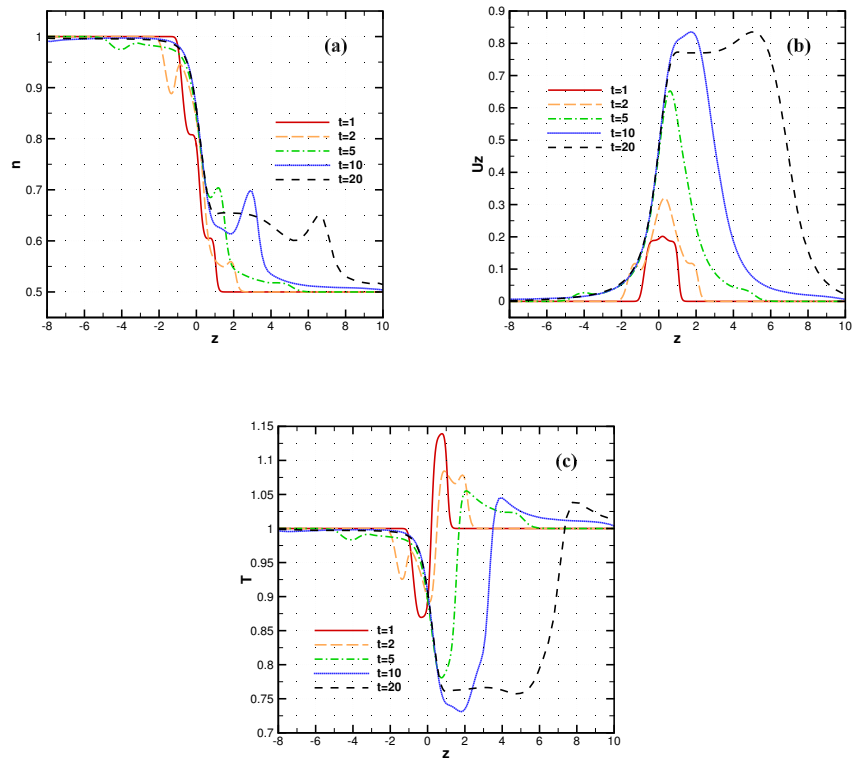


Figure 6: Distribution of density number (a), axial velocity (b), temperature (c) along the axis at several time moments for $p_1/p_0 = 0.5, \delta = 100$.

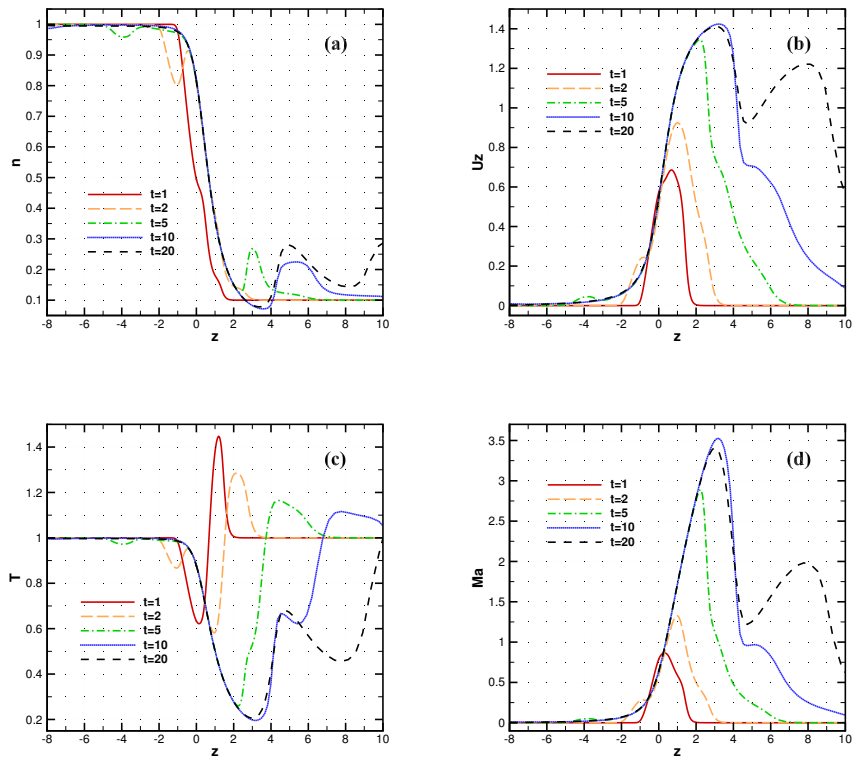


Figure 8: Distribution of density number (a), axial velocity (b), temperature (c), Mach number (d) along the axis at several time moments for $p_1/p_0 = 0.1, \delta = 100$.

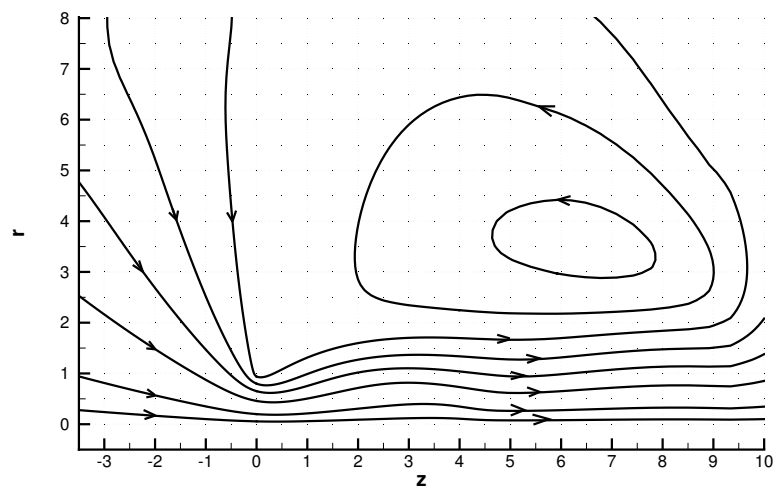


Figure 9: Stream lines at time moment $t = 20$ for $p_1/p_0 = 0.1, \delta = 100$.

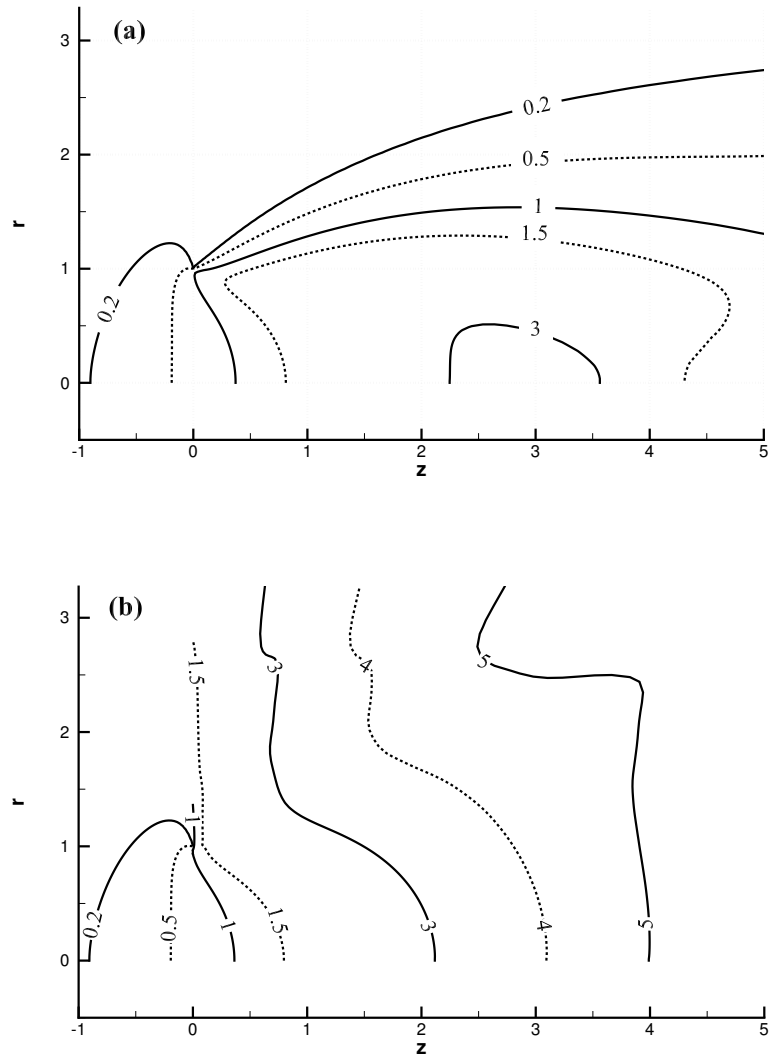


Figure 10: Mach number iso-lines at time moment $t = 20$ for $p_1/p_0 = 0.1, \delta = 100$. (a), $p_1/p_0 = 0., \delta = 100$. (b)

Figure 11: Dimensionless mass flow rate as a function of pressure ratio p_1/p_0 at different rarefaction parameters δ

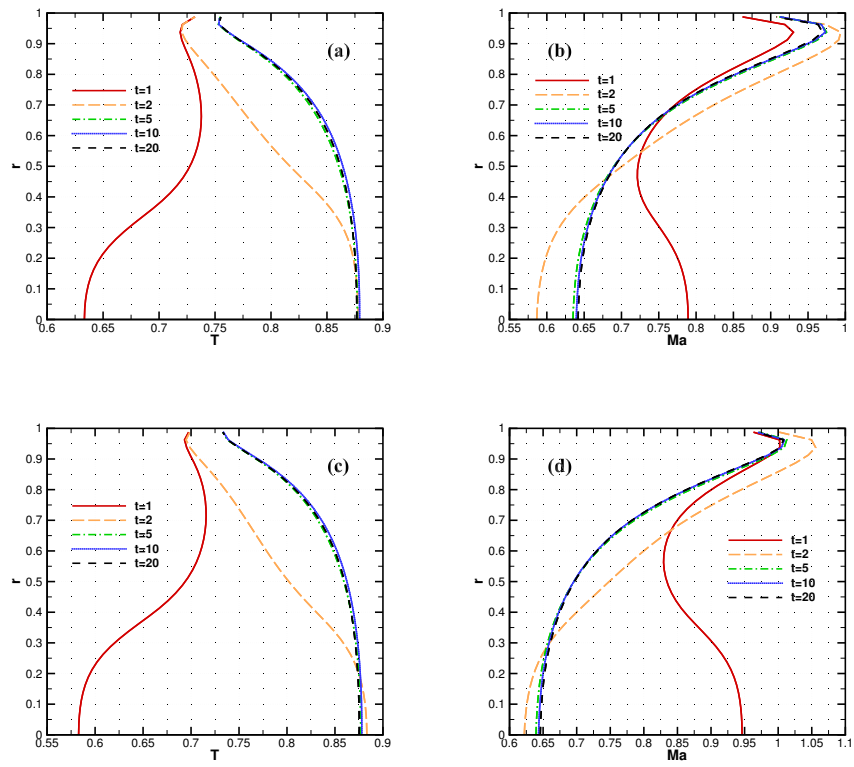


Figure 12: Distribution of temperature (a,c), Mach number (b,d) along the orifice at several time moments for $p_1/p_0 = 0.1, \delta = 100$. (a,b), $p_1/p_0 = 0., \delta = 100$. (c,d)

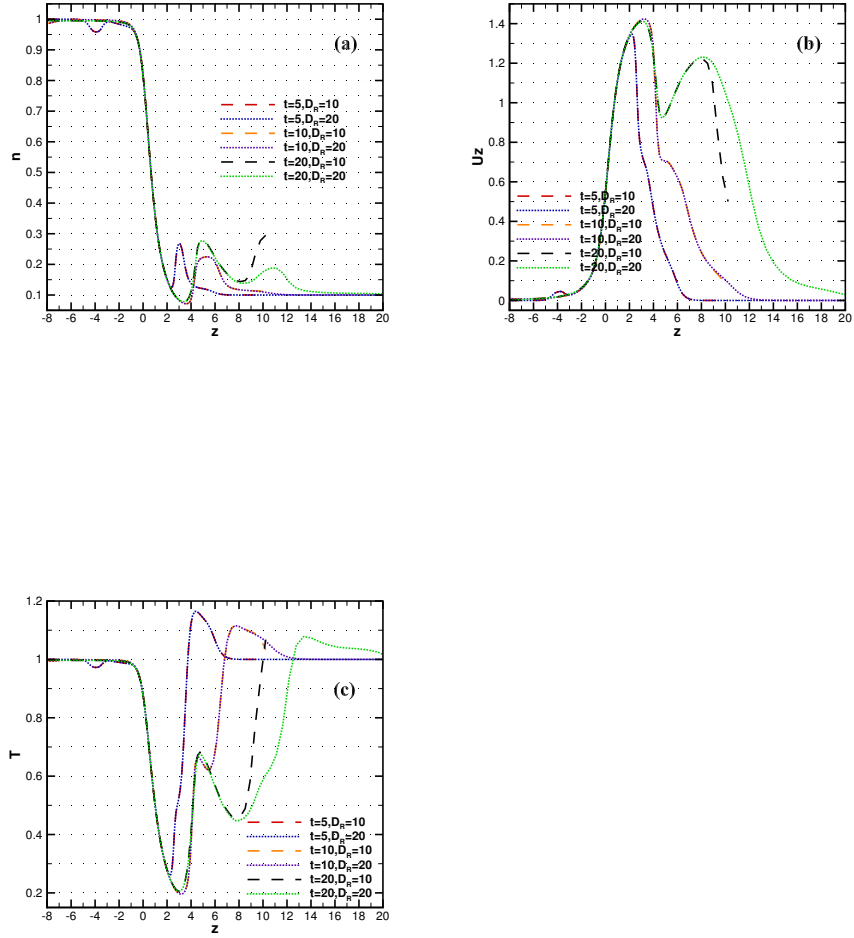


Figure 13: Distribution of density number (a), axial velocity (b), temperature (c) along the axis at time moments $t = 5, 10, 20$ for $p_1/p_0 = 0.1, \delta = 100$. with different computational domain sizes $D_R = 10, 20$. The time evolution of mass flow rate W with different computational domain sizes $D_R = 10, 20$ (d)